

A Triphasic Bifunctional Oxygen Electrocatalyst with Tunable and Synergetic Interfacial Structure for Rechargeable Zn-Air Batteries

Jianbing Zhu, Meiling Xiao, Gaoran Li, Shuang Li, Jing Zhang, Guihua Liu, Lu Ma, Tianpin Wu, Jun Lu, Aiping Yu, Dong Su, Huile Jin, Shun Wang,* and Zhongwei Chen*

Atomic-scale design of interfacial structure is an intriguing but challenging approach to developing efficient heterogenous catalysts for bifunctional oxygen electrocatalysis. Herein, an exquisite triphasic interfacial structure featuring the encapsulation of Fe_xNi alloy in a graphitic shell with a partial exposure of the FeO_y thin-layered surface is manipulated via an electronic modulation strategy. The spontaneous integration of well-crystallized metal alloy, carbon shell with a tunable active FeO_y layer, not only guarantees smooth charge transfer across the thin oxide layer, but also generates the synergistic effect at the interface, thus dramatically boosting the intrinsic activity of oxygen catalysis. Benefiting from these attributes, the hybrid catalyst outperforms the commercial noble-metal benchmarks with a higher half-wave potential of 0.890 V for oxygen reduction reaction and lower overpotential of 308 mV at 10 mA cm⁻² for the oxygen evolution reaction in alkaline media. Beyond that, a high-performance rechargeable Zn-air battery is realized with a narrow voltage gap of 0.742 V and excellent cyclability over 500 cycles at 10 mA cm⁻², demonstrating the great potential of the as-developed triphasic electrocatalyst for practical applications.

1. Introduction

Oxygen electrocatalysis, typically involving the heterogenous oxygen reduction reaction (ORR) and oxygen evolution reaction (OER) on catalytic solid surface, plays critical roles in metal-air battery chemistry.^[1] However, the sluggish kinetics of these proton-involved multistep-electron-transfer reactions determine that ORR and OER need be well catalyzed to overcome the large-overpotential and low energy efficiency, thus to fulfill a fast, efficient, and durable conversion between chemical and electrical energies.^[2] Therefore, high-performance and cost-effective electrocatalyst has always been the research focus in this field. During the past few decades, tremendous efforts have been devoted in pursuit of effective ORR and OER catalysts, yet highly efficient, low-cost, and robust bifunctional catalytic materials are still missing with their development remained challenging.^[3]

Generally, the activity of a heterogenous electrocatalytic reaction is highly subject to the surface/interface properties of the catalyst, which not only determines the adsorption strength toward the intermediates, but also affects the charge and mass transfer behaviors.^[4] Given this, rational regulation on the interface structure of heterogenous catalysts is regarded as a promising approach to boosting the intrinsic electrocatalytic activity. For instance, metal/metal oxide and oxide/oxide heterogenous structures^[5] have shown enhanced ORR/OER catalytic property due to the modulation of the binding strength between the intermediates and catalyst as a result of strong electronic interactions occurring on the interface. Additionally, manipulation on the carbon/metal interface^[1c,6] was reported with significant improvement in intrinsic activity attributed to a proposed electron penetration effect that activates the inert surface carbon. In spite of the considerable progress, several issues still remain to be well addressed: i) the poor conductivity of metal oxides impedes the release of their intrinsic activity completely; ii) the concurrent fulfillment of both good ORR and OER performance by a single catalyst is still challenging probably ascribed to the difficulty in balancing the adsorption-desorption kinetics for different reaction directions; iii) the tight contact between the interface components need be well maintained to guarantee the

Dr. J. Zhu, Dr. H. Jin, Prof. S. Wang
College of Chemistry and Materials Engineering
Wenzhou University
Wenzhou, Zhejiang 325035, China
E-mail: Shunwang@wzu.edu.cn

Dr. J. Zhu, Dr. M. Xiao, Dr. G. Li, Dr. J. Zhang, Dr. G. Liu,
Prof. A. Yu, Prof. Z. Chen
Department of Chemical Engineering
University of Waterloo
Waterloo, Ontario N2L 3G1, Canada
E-mail: zhwen@uwaterloo.ca

Dr. S. Li, Dr. D. Su
Centre for Functional Nanomaterials
Brookhaven National Laboratory
Upton, NY 11973, USA

Dr. L. Ma, Dr. T. Wu
X-Ray Science Division
Argonne National Laboratory
Lemont, IL 60439, USA

Dr. J. Lu
Chemical Sciences and Engineering Division
Argonne National Laboratory
Lemont, IL 60439, USA

 The ORCID identification number(s) for the author(s) of this article can be found under <https://doi.org/10.1002/aenm.201903003>.

DOI: 10.1002/aenm.201903003

structural and catalytic stability; and iv) the lack of insights and effective strategies that could power precise and controllable interface regulations at atomic level is obstructing the rational material designs with high electrocatalytic performance. Therefore, atomically controllable manipulation on the interfacial structure to well manage the intrinsic activity, electronic conductivity, and stability as well as gaining in-depth understanding on the underlying mechanism are highly requirable.

Herein, we developed a novel electronic modulation strategy to precisely manipulate an Fe_xNi alloy-Fe oxide-nitrogen doped graphitic carbon ($\text{Fe}_x\text{Ni-FeO}_y\text{-NC}$) triphase interfacial structure towards well-managed electronic conductivity, site density, and interfacial electronic interaction. The simple Ni doping can regulate the Fe oxidation degree to form adjustable FeO_y active surface layer specifically at the exposed surface area, which can balance the conductivity and exposed site density to guarantee the full expression of intrinsic activity as well as improve utilization of active sites. Besides, the electronic interaction occurring at interface could cooperatively boost the intrinsic activity. In addition, the subunits were further interconnected by continuous graphitic carbons to ensure fast long-range charge transfer. Consequently, the optimized catalyst exhibited outstanding electrocatalytic properties in terms of half-wave potential of 0.890 V for ORR and overpotential at 10 mA cm^{-2} of 308 mV for OER, surpassing the commercial noble-metal catalysts (Pt/C+Ir/C) and most of the reported noble-metal-free catalysts. The superior catalytic performance was further confirmed by Zn-air battery test, which showed a low charge–discharge voltage gap of 0.742 V and long lifetime over 500 cycles.

2. Results and Discussion

2.1. Interfacial Structure Evolution

The triphase interfacial structure was fabricated by an electronic modulation strategy via direct pyrolysis of Prussian-blue-analogue anchored on carbon nanotubes (PBA@CNTs) in composite with melamine, as illustrated in Figure S1 in the Supporting Information. PBA nanocrystals were first in situ grown on the surface of functionalized CNTs, which not only avoids the aggregation of PBA, but also interconnects the subunit to facilitate the long-range charge transfer for the obtained composite. The uniform dispersion of PBA nanocrystals in size of 20–30 nm on CNTs was confirmed by scanning electron microscopy (SEM) as shown in Figure S2 in the Supporting Information. Then, the PBA@CNTs hybrid was mixed with melamine and subsequently subject to pyrolysis under Ar atmosphere. The melamine serves as additional nitrogen and carbon sources, which decomposes and generates cyano environment (e.g., C_2N_2^+ , C_3N_2^+ , and C_3N_3^+) during the thermal treatment to implement the partial encapsulation of N-doped graphitic carbon on the Fe_xNi surface. Upon exposure to air, the uncovered Fe_xNi was spontaneously and selectively oxidized to form a highly adjustable FeO_y surface layer due to the stronger affinity of Fe to oxygen compared with Ni, thus contributing to the desired metal alloy-oxide-carbon ($\text{Fe}_x\text{Ni-FeO}_y\text{-NC}$) triphase interfacial structure. The incorporation of Ni not only regulates

the thickness of active FeO_y surface layer to balance the exposed active site density and the electronic conductivity, but also modulates the electronic structure of FeO_y through the interfacial charge transfer effect to boost the intrinsic catalytic activity (Figure 1a). With the rational management of active site density, conductivity and intrinsic activity, the as-prepared catalyst, denoted as $\text{Fe}_2\text{Ni@NC}$, delivers great promise in significantly boosting the catalytic performance for oxygen redox reactions. To elucidate the crucial role of Ni incorporation in regulating the triphase interfacial structure, catalysts derived from precursors with different Fe/Ni ratios (denoted as FeNi@NC and Fe@NC) were investigated for comparison (Table S1, Supporting Information).

The X-ray diffraction (XRD) patterns confirm the successful conversion of the pristine PBA crystals into metallic catalysts after pyrolysis (Figure S3, Supporting Information and Figure 1b). In addition to the peak of (002) facet of graphitic carbon at 26.3° , predominated diffraction peaks attributable to Fe_xNi alloy and Fe are clearly observed in the case of $\text{Fe}_x\text{Ni@NC}$ and Fe@NC , respectively. The strong intensity of these peaks suggests a good carbon graphitization (also confirmed by the relatively low I_d/I_g values in Raman spectra in Figure 1c) as well as the high crystallinity of the obtained Fe_xNi alloy or Fe, which guarantees a good electronic conductivity of the final catalysts. Apart from that, another small diffraction peak can be perceived in the XRD pattern of the as-prepared catalysts, which is attributed to the FeO_y ($\approx 35^\circ$ and 40°). Notably, this peak continuously weakens along with the decrease of Fe/Ni ratio, and is significantly lower than that in Ni-free Fe@NC pattern. This result strongly suggests that the incorporation of Ni into Fe is capably of linearly lessening the oxidation of Fe, thus realizing an adjustable FeO_y layer that facilitate the optimization of the metallic-carbon-oxide triphase interfacial structure for oxygen catalysis.

The morphological structure of the obtained catalysts was examined by SEM and transmission electron microscopy (TEM). A 3D porous hybrid structure can be observed for $\text{Fe}_2\text{Ni@NC}$ with highly intertwined CNTs as shown in Figure S4a, b in the Supporting Information. Meanwhile, the TEM image clearly confirms the crosslinking between CNTs, which uniformly anchors abundant $\text{Fe}_x\text{Ni-FeO}_y\text{-NC}$ subunits (Figure S4c, Supporting Information). This hierarchical configuration constructed by CNTs and the in situ grown graphitic carbons not only favors the transfer of reactants, such as OH^- and H_2O , to the catalytic sites, but also ensures a fast electron conduction within both short and long range for facilitated catalysis process. The porous structure of $\text{Fe}_2\text{Ni@NC}$ was also investigated by Brunauer–Emmett–Teller (BET) technique, which reveals a micro/mesoporous structure with a high surface area of $287 \text{ m}^2 \text{ g}^{-1}$ (Figure S5, Supporting Information). Deeper structural information of the as-developed material was further collected by high-resolution TEM (HRTEM). As shown in Figure 2a and Figure S4d in the Supporting Information, an FeO_y island layer can be found decorating on the Fe_2Ni alloy surface, which was confirmed by the fast Fourier transformation (FFT) pattern at the respective area as shown in Figure 2b,c. The scanning transmission electron microscopy coupled with electron energy-loss spectroscopy elemental mapping was performed to further elucidate the component distribution on the

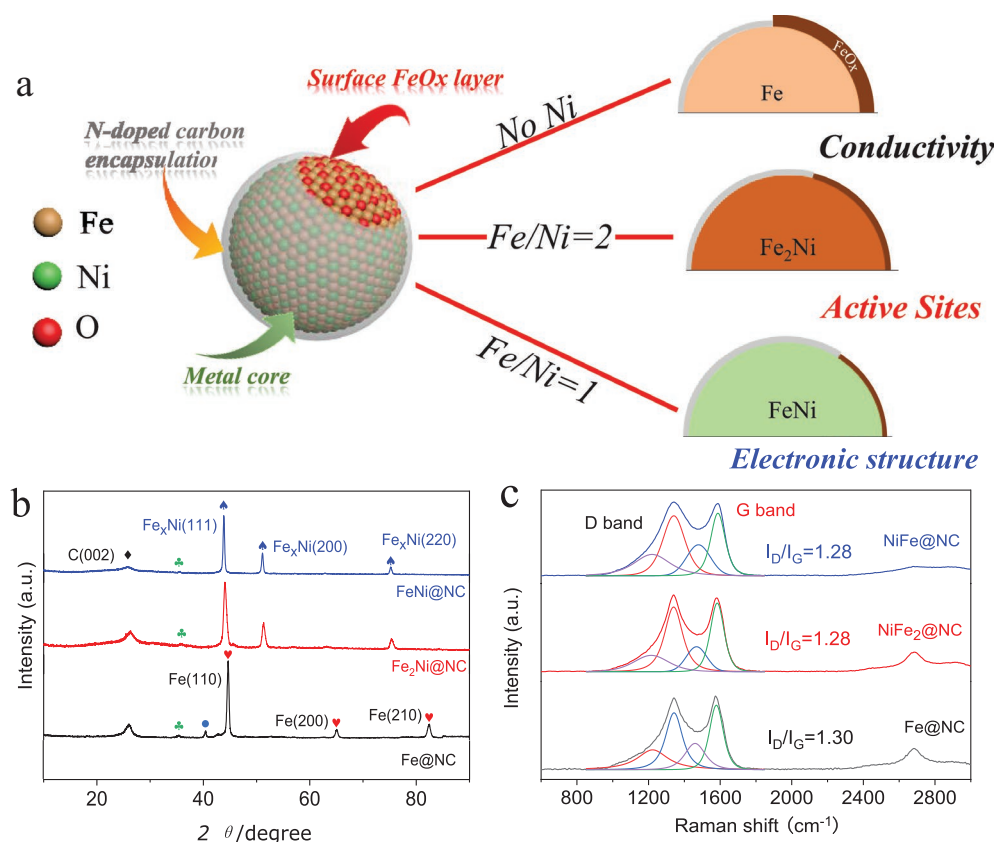


Figure 1. a) Schematic illustration for the synthesis of Fe₂Ni@NC catalysts, b) XRD, and c) Raman spectra of Fe@NC, Fe₂Ni@NC, and FeNi@NC.

metallic nanoparticle, which clearly identifies the Fe₂Ni alloy core, partial carbon wrapping, and the exposure of FeO_y layer, providing a strong evidence for the exquisite triphase interfacial structure of the as-developed Fe₂Ni@NC catalyst (Figure 2d–k). As for the sample without the Ni modulation, i.e., Fe@NC, similar hybrid morphology can be also obtained as shown in Figure S6 in the Supporting Information. However, the HRTEM shows its much thicker FeO_y shell in contrast to those of Fe₂Ni@NC (≈1.4 nm, Figure 2a) and FeNi@NC (≈1.2 nm, Figure S7, Supporting Information), which could severely obstruct electron transfer during electrochemical process. These results indicate the key role of Ni modulation on the oxidation behavior of Fe upon the construction of triphase interfacial catalysts.

Furthermore, the electronic modulation effect of Ni on the triphase interfacial structure was investigated by X-ray photoelectron spectroscopy (XPS), X-ray absorption near edge structure spectroscopy (XANES), and extend X-ray absorption fine structure (EXAFS) spectroscopy analysis. The XPS survey spectra confirm the presence of C, N, O, Fe, and Ni elements in the Ni-modulated samples as well as the absence of Ni in Fe@NC (Figure 3a). High-resolution N 1s XPS spectra of Fe₂Ni@NC (Figure S8a–c, Supporting Information) can be deconvoluted into four subpeaks including pyridinic N (398.9 eV), pyrrolic N (399.5 eV), graphitic N (400.9 eV), and oxidized N (402.6 eV). Similar N species can be also detected for the Fe@NC and FeNi@NC sample (Table S2, Supporting Information). The incorporation of N in the carbon lattice can increase the charge density and spin density of the adjacent C atoms, which not

only favors a higher electrical conductivity but also contribute partially to the ORR activity enhancement.^[7] Figure 3b shows the Fe 2p high-resolution spectra of the synthesized samples. The prominent peak at 707.4 eV is assigned to metallic iron, while the peak centered at 709 and 710.9 eV is ascribed to the Fe²⁺ and Fe³⁺, respectively, corresponding to FeO_x species. A strong dependence of ionic Fe intensity on initial Fe/Ni ratios can be perceived in the XPS analysis, where the incorporation of Ni decreases the intensity of the characteristic peaks for ionic Fe, in other words, slows down the oxidation of Fe. More interesting is that the ionic Fe tends to be higher valence state when decreasing Fe/Ni ratios, despite the suppressed Fe oxidation content (Table S3, Supporting Information). Since the oxygen reactivity is highly dependent on the electronic structure of the surface ionic species, the proper tuning on which can further increase the intrinsic activity. This suggests a facile strategy of manipulating an ideal triphase interfacial structure with controllable active species density, conductivity, and tailored electronic structure by simply adjusting the Fe/Ni ratios in precursor. Figure S8d in the Supporting Information displayed the Ni 2p spectra of Fe₂Ni@NC and FeNi@NC, in which no distinguishable peak of Niⁱⁱ can be found except for the metallic Ni, confirming the selective oxidation of Fe on Fe_xNi alloy in consistency with the TEM results. Further evidence for the electronic modulation effect of Ni can be obtained from the XANES analysis benefiting from its higher sensitivity to the valence state and coordination environment of the central atom. Obviously, the Fe K-edge XANES spectra show that the

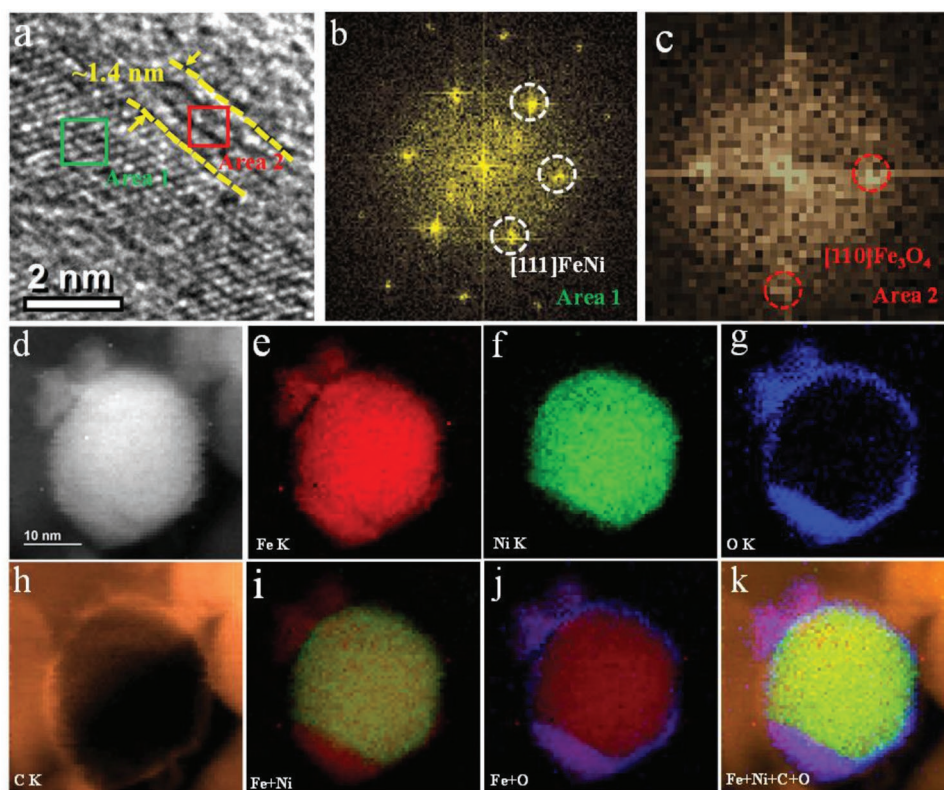


Figure 2. a) HRTEM, b, c) FFT patterns derived from area 1 and 2 regions in a); d–k) aberration-corrected EELS elemental maps of $\text{Fe}_2\text{Ni}@NC$, e) Fe, f) Ni, g) O, h) C, and overlaid of i) Fe, Ni signal, j) Fe, O signal, and k) Fe, Ni, C, and O signal.

energy absorption threshold value of $\text{Fe}_2\text{Ni}@NC$ is higher than that of Fe foil and lower than that of Fe_2O_3 , in consistent with the co-existence of metallic Fe_2Ni alloy and FeO_y as observed in TEM and XRD (Figure 3c). By contrast, the $\text{Fe}@NC$ displayed a positive shift of absorption energy compared with $\text{Fe}_2\text{Ni}@NC$ in Fe K-edge XANES spectra, implying the easier Fe oxidation in absence of Ni. Correspondingly, the white line intensity of Fe K-edge in $\text{Fe}_2\text{Ni}@NC$ is slightly higher than that in the Fe foil, but lower than those in the Fe_2O_3 and $\text{Fe}@NC$. When further decreasing the Fe/Ni ratio to 1/1, the $\text{FeNi}@NC$ catalyst exhibits a slightly lower intensity compared with $\text{Fe}_2\text{Ni}@NC$, suggesting the lower oxidation state of Fe.

As for the Ni K-edge XANES, both $\text{Fe}_2\text{Ni}@NC$ and $\text{FeNi}@NC$ displayed similar curves to Ni foil, demonstrating the metallic state of Ni in the as-prepared catalyst. The chemical states of Fe and Ni in the catalysts were also studied by the FT of EXAFS spectra, which provide abundant information on the first shell (M–O) and second shell (Fe–Fe, Fe–Ni, or Ni–Ni), the bond length and the coordination number. An additional peak at 1.7 Å can be observed corresponding to Fe–O path in the FT-EXAFS spectra Fe K-edge for the obtained catalysts in contrast to Fe foil (Figure S9, Supporting Information). It is noted that the Fe–O coordination number in $\text{Fe}_x\text{Ni}@NC$ and $\text{Fe}@NC$ was much smaller than that in FeO or Fe_2O_3 (Figure 3e–f and Table S4, Supporting Information), suggesting that only a small fraction of Fe on the surface was oxidized. The prominent peak in the spectra of $\text{Fe}_2\text{Ni}@NC$, $\text{FeNi}@NC$, and $\text{Fe}@NC$ is located at around 2.2 Å corresponding to Fe–Fe/Ni scattering with the

average bond length of ca. 2.50, 2.52, and 2.47 Å, respectively. The slightly larger bond length of $\text{Fe}_x\text{Ni}@NC$ than that in $\text{Fe}@NC$ sample confirms the Fe_xNi alloy characteristics. Accordingly, in Ni K-edge FT-EXAFS spectra (Figure S10, Supporting Information), both $\text{Fe}_2\text{Ni}@NC$ and $\text{FeNi}@NC$ samples consistently exhibit a predominant peak centered at a slightly negative R-space compared with that in Ni foil resulting from the evolution of Fe_xNi alloy.

This series of structural characterizations strongly demonstrate that the incorporation of Ni is capable of adjusting the oxidation degree of surface Fe as well as the electronic structure of the in situ formed iron oxide, thereby contributing to the tunable $\text{Fe}_x\text{Ni}-\text{FeO}_y\text{-NC}$ triphase interfacial structure. In-depth understanding on the evolution mechanism was further investigated by density functional theory calculations. Commonly, a phase change will occur on the Fe surface during the oxidation process, i.e., from metallic iron phase to the iron oxide phase. Therefore, we employed Fe vacancy formation energy (E_f) to evaluate the complexity to be oxidized (Figure 4). As the E_f of Fe vacancy decreases, the surface structure will be destroyed by easily.^[8] Obviously, Fe_2Ni (111) surface displays a much higher Fe vacancy formation energy than Fe (110), revealing that the oxidation was suppressed by alloying with Ni. Furthermore, we found that it becomes more difficult to form Ni vacancy compared with Fe vacancy on the Fe_2Ni (111) surface by showing a much higher E_f of Ni (3.33 eV), corresponding to the formation of Ni-free oxide on the surface. These calculation results were in line with the decreased FeOx portion in the

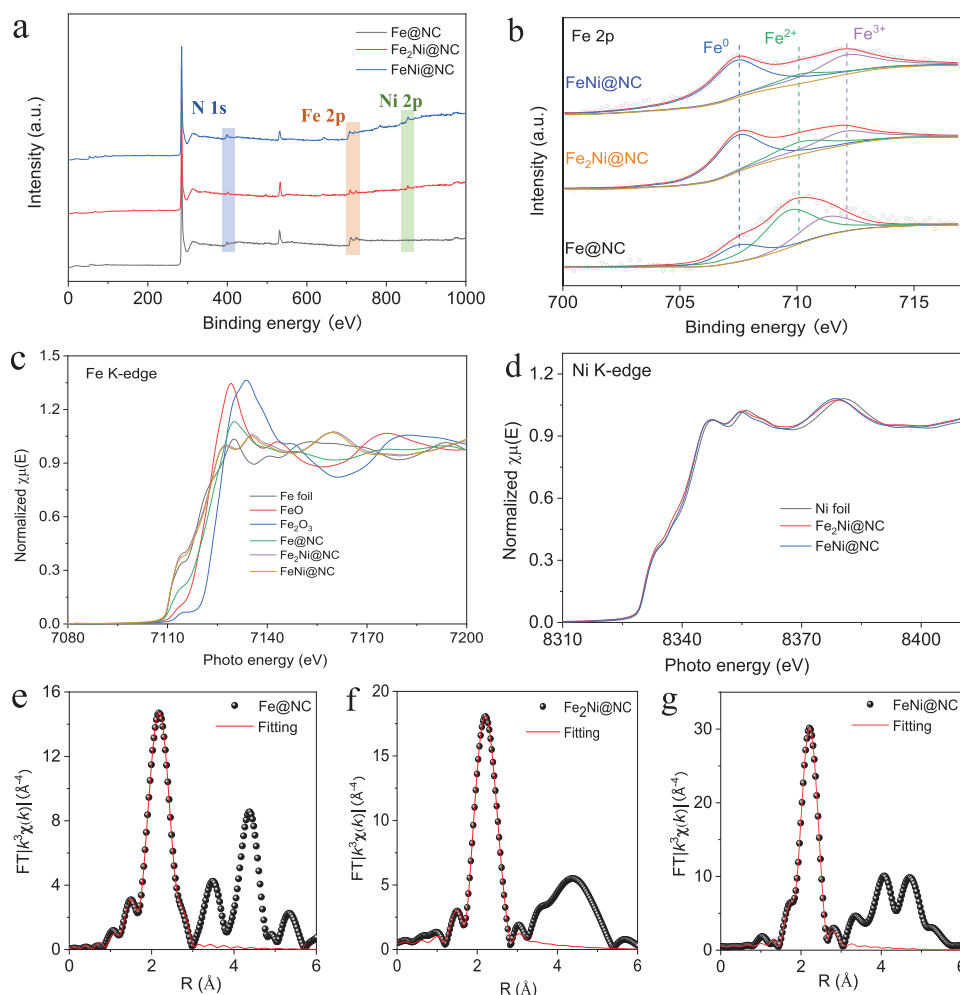


Figure 3. a) The survey and b) high-resolution XPS of Fe@NC, Fe₂Ni@NC, and FeNi@NC samples; c) Fe, d) Ni K-edge XANES spectra; corresponding Fourier transform k^3 -weighted $\chi(k)$ -function of the EXAFS spectra and corresponding EXAFS fitting curves at R space of e) Fe@NC and f) Fe₂Ni@NC, and g) FeNi@NC.

derived tri-phase interfacial structure upon Ni doping. To further investigate the interfacial electronic effect on the surface FeO_y, we examined the electronic structure of the separated surface Fe atom. In partial density of state (PDOS) of the separated Fe atom, it can be found that the d-band center of separated Fe on Fe₂Ni is closer to Fermi level than that of Fe. This indicates that separated Fe atom on Fe₂Ni will show stronger affinity to the other O atoms, therefore, the separated Fe atom shows higher valence state in the oxidant layers on Fe₂Ni, in consistent with the XPS analysis that the binding energy of Fe in surface FeO_y shifts to higher energy. Consequently, this will lead to enhanced intrinsic activity as the higher valence state Fe species have been regarded more active to catalyze oxygen redox reaction.^[9]

2.2. Catalytic Performance

To assess the bifunctional catalytic activity, the ORR and OER performances based on the obtained catalysts were evaluated in a typical three-electrode electrochemical cell by steady-state

linear sweep voltammetry in 0.1 M KOH electrolyte at a rotating speed of 1600 rpm. To demonstrate the superiority of the well-designed interfacial structure, Fe@NC and FeNi@NC were also investigated for comparison. Besides, the state-of-the-art Pt/C and Ir/C catalysts were measured as ORR and OER benchmarks, respectively. All potentials are provided versus reversible hydrogen electrode. As shown in Figure 5a and Table S5 in the Supporting Information, Fe₂Ni@NC delivers the highest ORR activity by showing more positive onset potential (E_{onset}) of 1.02 V and half-wave potential ($E_{1/2}$) of 0.89 V than those of Fe@NC (E_{onset} : 0.98 V and $E_{1/2}$: 0.84 V) and FeNi@NC (E_{onset} : 1.0 V and $E_{1/2}$: 0.87 V). This is attributed to the optimal FeO_y portion in the Fe₂Ni@NC and the interfacial electronic transfer between Fe₂Ni alloy and FeO_y, which not only overcomes the intrinsically poor conductivity of metal oxide-based catalysts, but also boosts the intrinsic activity synergistically. Besides, the electronic modulation effect of Fe₂Ni core can activate the surface graphitic carbon and thus further contributes to electrocatalytic activity.^[6g,10] It should be noted that the optimal catalyst, Fe₂Ni@NC also outperforms the commercial Pt/C catalyst and most of the reported non-precious metal catalysts (NMPCs) in

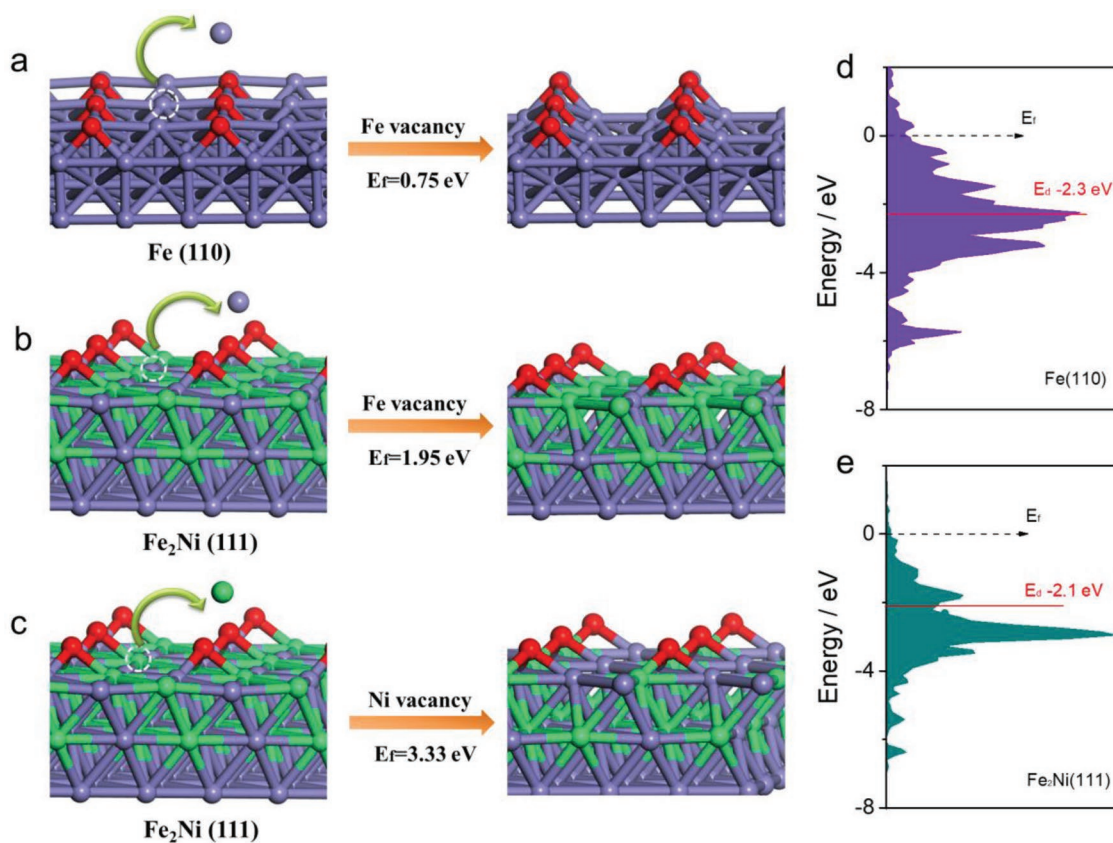


Figure 4. a) Fe atom vacancy formation energy on Fe (110) surface; b) Fe, c) Ni vacancy formation energy on Fe₂Ni (111) surface; and d,e) Fe 3d PDOS of surface oxidized Fe atoms.

catalyzing ORR (Table S6, Supporting Information). The ORR catalytic selectivity was also evaluated by rotating ring disk electrode (RRDE) measurements as shown in Figure 5b. The H₂O₂ yield of Fe₂Ni@NC remains below 3.3% in the potential range 0.05–0.9 V corresponding to a high electron-transfer number of 3.93–4.00, which approaches the theoretical value for the 4e[−] ORR process. This result is in good agreement with the calculation based on the Koutecky–Levich (K-L) equations (Figure S11, Supporting Information). The H₂O₂ yield is even lower than that of Pt/C (Figure S12, Supporting Information). In comparison, the *n*-value is 3.85–4.00 and 3.79–4.00 for the FeNi@NC (Figure S13, Supporting Information) and Fe@NC (Figure S14, Supporting Information), respectively, indicating the easier access to the desirable four-electron ORR pathway on the Fe₂Ni@NC. Moreover, the enhanced ORR kinetics on Fe₂Ni@NC is also confirmed by the smaller Tafel slope of 43 mV dec^{−1} (Figure 5c) compared with those of FeNi@NC (52 mV dec^{−1}), Fe@NC (53 mV dec^{−1}), and Pt/C (52 mV dec^{−1}), further manifesting the superior ORR performance of Fe₂Ni@NC electrocatalyst. These results demonstrate the construction of triphasic interfacial structure with optimal surface oxide can efficiently improve ORR activity and accelerate ORR kinetics.

As for the OER activity, the Fe₂Ni@NC also outperformed all other comparison catalysts, with an onset overpotential (*E*_{onset}) of only 0.23 V and an overpotential to reach current den-

sity of 10 mA cm^{−2} (*E*_{*j*=10}) of only 0.308 V (Figure 5d). These values were significantly lower than those of the state-of-the-art Ir/C catalysts (*E*_{onset}: 0.238 V and *E*_{*j*=10}: 0.358 V, consistent with reported values), commercial IrO₂ black (*E*_{*j*=10}: 0.331 V, Figure S15, Supporting Information) and the leading NMPCs ever reported (Table S7, Supporting Information), manifesting its great promise in developing non-noble metal and cost-effective catalysts. The improved catalytic kinetics on Fe₂Ni@NC can be also confirmed by its lowest Tafel slope of 49 mV dec^{−1} for OER (Figure 5e). The bifunctional activity is assessed by the voltage difference between *E*_{1/2} for ORR and *E*_{*j*=10} for OER ($\Delta E = E_{j=10} - E_{1/2}$), where the smaller ΔE indicates the limited electrochemical polarization and better bifunctional activity. The thermodynamic potential (*E*_{o(OH[−]/O₂)} = 1.23 V) is used as the reference to reflect each overpotential with respect to ORR and OER. As depicted in Figure 5f, Fe₂Ni@NCx exhibits the smallest ΔE of ca. 0.648 V, which surpasses the commercial Pt/C–Ir/C catalysts and reported excellent bifunctional catalysts.^[11] Further evidence for the superior bifunctional activity of Fe₂Ni@NC is provided by its highest kinetic current density at fixed potentials for both ORR and OER, as shown in Figure 5g. Besides, the intrinsic activity was compared by normalized the kinetic current density to the electrochemically active surface areas, where Fe₂Ni@NC shows the highest intrinsic activity (Figures S16 and S17, Supporting Information). It

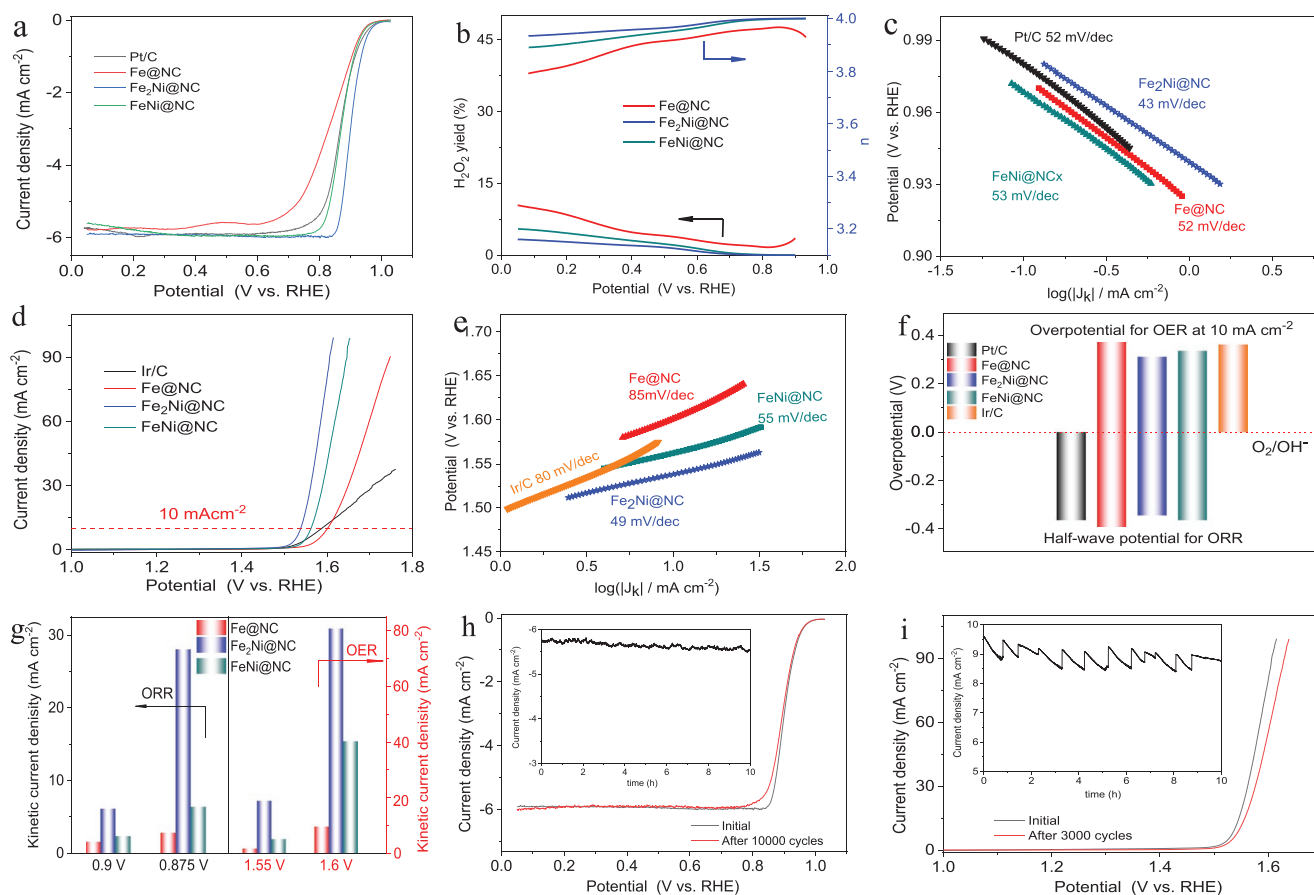


Figure 5. a) The ORR polarization curves of all samples in 0.1 M KOH solution; b) H_2O_2 yield and corresponding electron transfer number calculated by using RRDE method; c) Tafel plots for ORR; d) the OER polarization curves of all samples; e) Tafel plots for OER; f) potential differences between the $E_{1/2}$ of ORR and $E_{j=10}$ of OER for the as-prepared catalysts; g) kinetic current density of ORR and OER for the synthesized catalysts at fixed potentials for the as-prepared catalysts; h) ORR polarization plots of $\text{Fe}_2\text{Ni}@/\text{NC}$ catalysts before and after 10 000 potential cycles, inset shows the $i-t$ curve at 0.8 V; and i) OER polarization plots of $\text{Fe}_2\text{Ni}@/\text{NC}$ catalysts before and after 3000 potential cycles, inset shows the $i-t$ curve at 1.55 V.

should be noted that either increasing or decreasing the Ni portion in the precursor, the resultant $\text{FeNi}@/\text{NC}$ or $\text{Fe}@/\text{NC}$ demonstrate inferior catalytic activity to the optimal $\text{Fe}_2\text{Ni}@/\text{NCx}$. This is due to the balance among intrinsic activity, active site density and electronic conductivity achieved with a moderate Ni doping, which further reveals the critical role of interfacial structure in determining the final catalytic property.

Since the durability is another significant criterion particularly for practical applications, the obtained catalysts were further subject to accelerated durability tests (ADT) and chronoamperometry (CA) for stability evaluation. For ORR, the $\text{Fe}_2\text{Ni}@/\text{NC}$ catalyst shows only 5 mV negative shift in half-wave potential after 10 000 potential cycles (Figure 5h), whereas the counterpart commercial Pt/C catalyst shows a much higher shift of 13 mV (Figure S18, Supporting Information). The $\text{Fe}_2\text{Ni}@/\text{NC}$ also outperforms the $\text{Fe}@/\text{NC}$ and $\text{FeNi}@/\text{NC}$ catalysts (Figure S19, Supporting Information). Moreover, the Tafel slope of $\text{Fe}_2\text{Ni}@/\text{NC}$ after ADT test is close to its intimal value (Figure S20, Supporting Information). The excellent stability can be also supported by CA curve, where $\text{Fe}_2\text{Ni}@/\text{NC}$ retains 95.1% current after 10 h test in O_2 -saturated electrolyte, preponderant than that for the Pt/C catalyst (24% decay in

current density). Even under the harsh conditions for OER, the $\text{Fe}_2\text{Ni}@/\text{NC}$ also demonstrates impressive stability with a limited overpotential increase of 10 mV (to 0.318 V) to approach the current density of 10 mA cm^{-2} after 3000 continuous potential cycles, which is significantly smaller than that for commercial Ir/C catalyst (64 mV positive shift, Figure S21, Supporting Information). It should be noted that $\text{Fe}_2\text{Ni}@/\text{NC}$ also exhibits the highest stability among the $\text{Fe}@/\text{NC}$, $\text{FeNi}@/\text{NC}$, and $\text{Fe}_2\text{Ni}@/\text{NC}$ catalysts (Figure S22, Supporting Information). The CA profile also spotlights the prominent stability of $\text{Fe}_2\text{Ni}@/\text{NC}$ catalyst by showing well maintained current response upon the 10 h test (Figure 5i, inset). Furthermore, the Tafel slope of $\text{Fe}_2\text{Ni}@/\text{NC}$ after ADT test confirmed its superior stability (Figure S23, Supporting Information). The impressive electrochemical stability of $\text{Fe}_2\text{Ni}@/\text{NC}$ catalyst is probably ascribed to the tight contact of the well-designed triphase interfacial structure and the strong electronic coupling effect among them. The morphology and composition of $\text{Fe}_2\text{Ni}@/\text{NC}$ after the durability test is investigated (Figure S24, Supporting Information), which exhibit a retained morphology and a slight dissolution of surface Fe species after the harsh electrochemical process.

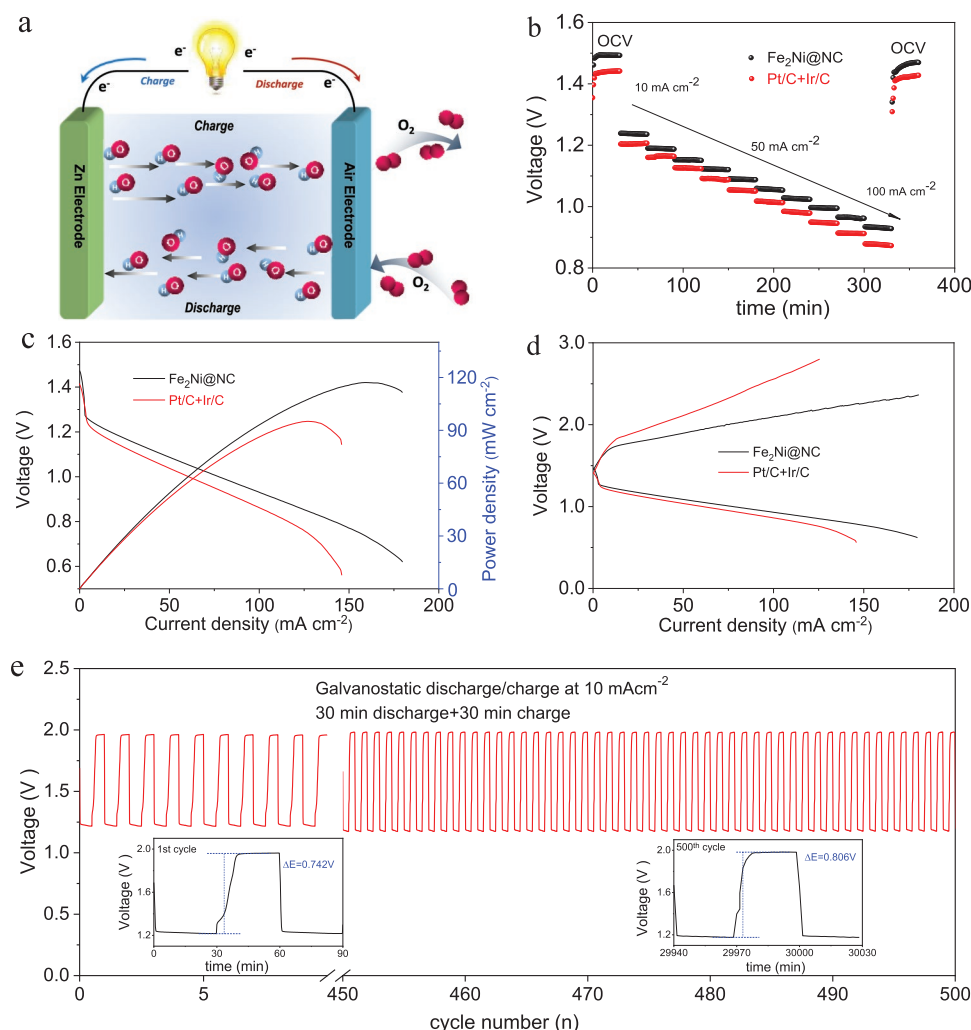


Figure 6. Performance of rechargeable Zn-air batteries based on of Fe₂Ni@NC catalyst and Ir/C+ Pt/C catalysts. a) Schematically depicts the structure of assembled rechargeable Zn-air batteries; b) polarization curves of the Zn-air batteries using Fe₂Ni@NC or Ir/C+ Pt/C as air electrode at different current density; c) polarization and power density curves of the Zn-air batteries using Fe₂Ni@NC or Ir/C+ Pt/C catalysts; d) charge and discharge polarization curves of the rechargeable Zn-air batteries use Fe₂Ni@NC and Ir/C+ Pt/C catalysts as cathode, respectively; and e) cycling performance of Zn-air batteries assembled using Fe₂Ni@NC as air electrodes with the galvanostatic discharge-charge current at 10 mA cm⁻² and a duration of 60 min per cycle.

2.3. Zn-Air Battery Test

To assess the practical applicability of the as-developed bifunctional Fe₂Ni@NC catalyst, a homemade single-cell Zn/air battery was fabricated consisting of a zinc plate as anode, a gas diffusion layer coated with Fe₂Ni@NC catalyst as cathode (Figure 6a). The Pt/C+Ir/C couple was also employed as the air cathode for comparative study. The cell with Fe₂Ni@NC cathode clearly exhibits a higher open-circuit voltage of 1.493 V than that based on Pt/C+Ir/C (1.441 V). Moreover, upon the current increase from 10 to 100 mA cm⁻², Fe₂Ni@NC cathode shows a constantly higher voltage with a smaller voltage fading of 0.505 V than Pt/C+Ir/C (0.569 V) (Figure 6b), signifying its superior rate capability. As illustrated in Figure 6c, the Fe₂Ni@NC-based battery outperforms that with Pt/C+Ir/C by yielding a significantly higher peak power density (126 mW cm⁻² versus 97 mW cm⁻²). Furthermore, the Fe₂Ni@NC exhibits admirable discharge capacities of 770 and 720 W h kg_{Zn}⁻¹ at 10 and

50 mA cm⁻² (Figure S25, Supporting Information), respectively, higher than the commercial noble metal counterpart and approaching to the theoretical capacity. Figure 6d displays the discharge and charge polarization curves for Zn/air batteries with Fe₂Ni@NC and Pt/C+Ir/C cathode. Obviously smaller charge-discharge voltage gap can be observed with Fe₂Ni@NC cathode compared with the commercial counterparts. Specifically, the charge-discharge voltage gap for the Fe₂Ni@NC cathode-based Zn-air battery is 0.805 V at a current density of 50 mA cm⁻², which is significantly lower than that of the Pt/C+Ir/C cathode (1.075 V), indicating the great capability of Fe₂Ni@NC catalyst in promoting the oxygen redox efficiency and kinetics. When cycled at a constant current density of 10 mA cm⁻², the Fe₂Ni@NC cathode-based battery shows an initial voltage gap of 0.742 V and a high round-trip efficiency of 62.1%. After 500 cycles, the Fe₂Ni@NC cathode undergoes only a slight performance loss with a small increase in the voltage gap by 0.064 V, whereas the commercial counterpart suffers from a severe increase in voltage

gap (0.123 V) after 50 cycles (Figure S26, Supporting Information). In order to quantify the variation of charge and discharge voltages with cycling, the voltage fading rate is calculated on both Fe₂Ni@NC and Pt/C+Ir/C electrodes, with an extremely low voltage fading rate of 0.128 mV per cycle on Fe₂Ni@NC, while the Pt/C+Ir/C counterpart exhibits a much severer degradation with voltage fading rate of 2.46 mV per cycle. The severe activity degradation of Pt/C+Ir/C benchmark is probably due to the dissolution and/or aggregation of noble metal nanoparticles as a result of carbon corrosion and Ostwald ripening. Besides, the metallic Pt nanoparticles tends to be oxidized in the charge process, leading to the formation of inactive PtO_x species. These results strongly demonstrate the superiority of the as-developed Fe₂Ni@NC catalyst in the development of highly durable zinc-air battery (Figure 6e, and Figure S26, Supporting Information). The home-made Zn-air battery can easily power a mini-fan, as illustrated in Figure S25c in the Supporting Information. These good performances in real battery evaluations reveal the intriguing potential of our catalyst in practical application.

3. Conclusion

In summary, we have developed an exquisite Fe_xNi-FeO_y-NC tri-phase interfacial structure by an electronic modulation strategy, in which Ni regulates the oxidation degree of Fe and contributes to an optimal FeO_y portion with tailored electronic structure on the surface. Benefiting from the interfacial charge transfer effect and the compositional optimization of interface structure, well-managed intrinsic activity, active site density, and conductivity can be achieved, leading to unprecedented catalytic activity and stability for oxygen electrocatalysis, with an ultrahigh half-wave potential of 0.890 V for ORR and low overpotential of 308 mV at $j = 10 \text{ mA cm}^{-2}$ for OER. Furthermore, when integrated within an air electrode, a low voltage gap of 0.742 V was achieved in the charge–discharge process with negligible activity decay after 500 cycles, revealing its promising application in practical Zn-air batteries.

Supporting Information

Supporting Information is available from the Wiley Online Library or from the author.

Acknowledgements

J.Z. and M.X. contributed equally to this work. The authors would like to acknowledge the financial support from the University of Waterloo and Wenzhou University. The Catalysis Research for Polymer Electrolyte Fuel Cells (CaRPE FC) Network administered from Simon Fraser University and supported by Automotive Partnership Canada (APC) grant no. APCP/417858–11 through the Natural Sciences and Engineering Research Council of Canada (NSERC) are greatly acknowledged. S.W. is grateful for financial support from the National Natural Science Foundation of China (51872209 and 51772219) and the Zhejiang Provincial Natural Science Foundation of China (LY17E02002). Electron microscopy work was performed at the Center for Functional Nanomaterials, Brookhaven National Laboratory, which is supported by the U.S. Department of Energy (DOE), Office of Basic Energy Science, under contract

no. DE-SC0012704. Research conducted at beamline 9-BM used resources of the Advanced Photon Source, an Office of Science User Facility operated for the U.S. Department of Energy (DOE) Office of Science by Argonne National Laboratory under contract no. DE-AC02-06CH11357. J.L. gratefully acknowledges support from the U. S. Department of Energy (DOE), Office of Energy Efficiency and Renewable Energy, and Vehicle Technologies Office. Argonne National Laboratory is operated for DOE Office of Science by UChicago Argonne, LLC, under contract no. DE-AC02-06CH11357. The authors also thank Dr. Yongfeng Hu and Dr. Qunfeng Xiao from Canadian Light Sources (CLS) for XAS data analysis. The CLS is supported by NSERC, the national Research Council Canada, the Canadian Institutes of Health Research, the Province of Saskatchewan, Western Economic Diversification Canada, and the University of Saskatchewan.

Conflict of Interest

The authors declare no conflict of interest.

Keywords

atomic regulation, bifunctional catalysts, electronic modulation, interfacial structures, Zn-air batteries

Received: September 12, 2019

Revised: November 17, 2019

Published online:

- [1] a) G. Li, X. Wang, J. Fu, J. Li, M. G. Park, Y. Zhang, G. Lui, Z. Chen, *Angew. Chem., Int. Ed.* **2016**, *55*, 4977; b) Z. P. Cano, D. Banham, S. Ye, A. Hintennach, J. Lu, M. Fowler, Z. Chen, *Nat. Energy* **2018**, *3*, 279; c) B. Y. Guan, L. Yu, X. W. Lou, *Energy Environ. Sci.* **2016**, *9*, 3092.
- [2] a) J. K. Nørskov, J. Rossmeisl, A. Logadottir, L. Lindqvist, J. R. Kitchin, T. Bligaard, H. Jonsson, *J. Phys. Chem. B* **2004**, *108*, 17886; b) C. C. L. McCrory, S. Jung, J. C. Peters, T. F. Jaramillo, *J. Am. Chem. Soc.* **2013**, *135*, 16977; c) F. Cheng, J. Chen, *Chem. Soc. Rev.* **2012**, *41*, 2172; d) V. Stamenković, T. J. Schmidt, P. N. Ross, N. M. Marković, *J. Phys. Chem. B* **2002**, *106*, 11970; e) N.-T. Suen, S.-F. Hung, Q. Quan, N. Zhang, Y.-J. Xu, H. M. Chen, *Chem. Soc. Rev.* **2017**, *46*, 337; f) T. Reier, M. Oezaslan, P. Strasser, *ACS Catal.* **2012**, *2*, 1765.
- [3] a) N. M. Marković, T. J. Schmidt, V. Stamenković, P. N. Ross, *Fuel Cells* **2001**, *1*, 105; b) Y. Jiao, Y. Zheng, M. Jaroniec, S. Z. Qiao, *Chem. Soc. Rev.* **2015**, *44*, 2060; c) Z. Chen, D. Higgins, A. Yu, L. Zhang, J. Zhang, *Energy Environ. Sci.* **2011**, *4*, 3167; d) J. Fu, Z. P. Cano, M. G. Park, A. Yu, M. Fowler, Z. Chen, *Adv. Mater.* **2017**, *29*, 1604685; e) J. Masa, A. Zhao, W. Xia, M. Muhler, W. Schuhmann, *Electrochim. Acta* **2014**, *128*, 271.
- [4] a) Y. P. Zhu, C. Guo, Y. Zheng, S.-Z. Qiao, *Acc. Chem. Res.* **2017**, *50*, 915; b) V. Stamenkovic, B. S. Mun, K. J. J. Mayrhofer, P. N. Ross, N. M. Markovic, J. Rossmeisl, J. Greeley, J. K. Nørskov, *Angew. Chem.* **2006**, *118*, 2963; c) S. Gupta, L. Qiao, S. Zhao, H. Xu, Y. Lin, S. V. Devaguptapu, X. L. Wang, M. T. Swihart, G. Wu, *Adv. Energy Mater.* **2016**, *6*, 1601198; d) G. Chen, Y. Zhao, G. Fu, P. N. Duchesne, L. Gu, Y. Zheng, X. Weng, M. Chen, P. Zhang, C.-W. Pao, J.-F. Lee, N. Zheng, *Science* **2014**, *344*, 495; e) G. Chen, C. Xu, X. Huang, J. Ye, L. Gu, G. Li, Z. Tang, B. Wu, H. Yang, Z. Zhao, Z. Zhou, G. Fu, N. Zheng, *Nat. Mater.* **2016**, *15*, 564; f) P. Z. Chen, Y. Tong, C. Z. Wu, Y. Xie, *Acc. Chem. Res.* **2018**, *51*, 2857.
- [5] a) Y. Jiang, Y.-P. Deng, J. Fu, D. U. Lee, R. Liang, Z. P. Cano, Y. Liu, Z. Bai, S. Hwang, L. Yang, D. Su, W. Chu, Z. Chen, *Adv. Energy*

- Mater.* **2018**, *8*, 1702900; b) S. Zhao, R. X. Jin, H. Abroshan, C. J. Zeng, H. Zhang, S. D. House, E. Gottlieb, H. J. Kim, J. C. Yang, R. C. Jin, *J. Am. Chem. Soc.* **2017**, *139*, 1077; c) K. Zhu, M. Li, X. Li, X. Zhu, J. Wang, W. Yang, *Chem. Commun.* **2016**, *52*, 11803.
- [6] a) Y. Lin, L. Yang, Y. Zhang, H. Jiang, Z. Xiao, C. Wu, G. Zhang, J. Jiang, L. Song, *Adv. Energy Mater.* **2018**, *8*, 1703623; b) M. L. Xiao, J. B. Zhu, L. G. Feng, C. P. Liu, W. Xing, *Adv. Mater.* **2015**, *27*, 2521; c) A. Aijaz, J. Masa, C. Rosler, W. Xia, P. Weide, A. J. R. Botz, R. A. Fischer, W. Schuhmann, M. Muhler, *Angew. Chem., Int. Ed.* **2016**, *55*, 4087; d) C.-Y. Su, H. Cheng, W. Li, Z.-Q. Liu, N. Li, Z. Hou, F.-Q. Bai, H.-X. Zhang, T.-Y. Ma, *Adv. Energy Mater.* **2017**, *7*, 1602420; e) J. Masa, W. Xia, I. Sinev, A. Zhao, Z. Sun, S. Grützkke, P. Weide, M. Muhler, W. Schuhmann, *Angew. Chem., Int. Ed.* **2014**, *53*, 8508; f) B. Y. Guan, L. Yu, X. W. Lou, *Angew. Chem., Int. Ed.* **2017**, *56*, 2386; g) J. Zhu, M. Xiao, Y. Zhang, Z. Jin, Z. Peng, C. Liu, S. Chen, J. Ge, W. Xing, *ACS Catal.* **2016**, *6*, 6335.
- [7] a) L. Zhang, Z. Xia, *J. Phys. Chem. C* **2011**, *115*, 11170; b) K. Gong, F. Du, Z. Xia, M. Durstock, L. Dai, *Science* **2009**, *323*, 760; c) D. Guo, R. Shibuya, C. Akiba, S. Saji, T. Kondo, J. Nakamura, *Science* **2016**, *351*, 361.
- [8] M. C. S. Escaño, H. Kasai, *J. Power Sources* **2014**, *247*, 562.
- [9] J. Y. C. Chen, L. N. Dang, H. F. Liang, W. L. Bi, J. B. Gerken, S. Jin, E. E. Alp, S. S. Stahl, *J. Am. Chem. Soc.* **2015**, *137*, 15090.
- [10] X. J. Cui, P. J. Ren, D. H. Deng, J. Deng, X. H. Bao, *Energy Environ. Sci.* **2016**, *9*, 123.
- [11] a) Y. Tong, P. Chen, T. Zhou, K. Xu, W. Chu, C. Wu, Y. Xie, *Angew. Chem., Int. Ed.* **2017**, *56*, 7121; b) T. Ling, D.-Y. Yan, Y. Jiao, H. Wang, Y. Zheng, X. Zheng, J. Mao, X.-W. Du, Z. Hu, M. Jaroniec, S.-Z. Qiao, *Nat. Commun.* **2016**, *7*, 12876; c) J. Fu, F. M. Hassan, C. Zhong, J. Lu, H. Liu, A. Yu, Z. Chen, *Adv. Mater.* **2017**, *29*, 1702526.